Moment Capacity Assessment of Hybrid GFRP-Steel Reinforced Concrete Beams

Vui Van Cao[*1,2], Khanh Ba Le[1,2], Det Van Doan[1,2]

[1] Faculty of Civil Engineering, Ho Chi Minh City University of Technology (HCMUT), 268 Ly Thuong Kiet Street, Dien Hong Ward, Ho Chi Minh City, Vietnam.

[2] Vietnam National University Ho Chi Minh City (VNU-HCM), Linh Xuan Ward, Ho Chi Minh City, Vietnam.

[*] Corresponding author's Email: cvvui@hcmut.edu.vn

Abstract: Combinations of fiber-reinforced polymer (FRP) bars and steel bars to reinforce concrete structures appear an advanced solution, as it combines the advantages of both materials. Research effort has been devoted to steel reinforced concrete (RC) and FRP RC structures, while it has been limited for hybrid FRP-steel RC structures. This study thus aims at assessment of moment–curvature behavior and ultimate moment of hybrid glass FRP (GFRP)-steel RC beam sections. To achieve this aim, fiber models were developed to model beam sections reinforced with different GFRP-steel combinations. These combinations are expressed by the ratio of the GFRP area to the total area of GFRP and steel, namely $\rho_{f/fs}$, which varies from 0 to 1. The fiber models were verified by comparing with the experimental results with satisfactory agreement. The verified models were then used for parametric investigations considering the effect of concrete strength, steel strength, FRP strength, and $\rho_{f/fs}$ on the behavior and ultimate moment capacity of hybrid GFRP-steel beam sections. When $\rho_{f/fs}$ increases from 0 to 1, the bilinear response transitions to a linear response, and the ultimate moment increases. The pivot point is a phenomenon of the moment–curvature curves when $\rho_{f/fs}$ varies from 0 to 1. Concrete with higher compressive strength, which delays the compression failure, more effectively exploits the tensile strength of GFRP bars. GFRP bars effectively replace low-strength steel bars, resulting in a higher ultimate moment. Multivariate regression analysis was performed, and the established model indicates that the considered parameters exhibit positive effects on the ultimate moment.

Keywords: Beam, GFRP-steel reinforcement, Moment capacity, Parametric study, Reinforced concrete

1 Introduction

Steel reinforced concrete (RC) has been a traditional material in construction. However, corrosion of steel during operational time has substantially downgraded structures [1]. The corrosion of steel increases the volume many times, resulting in internal stress and then spalling of the concrete.

Fiber-reinforced polymer (FRP) is a material that offers a solution for the corrosion issue. FRP possesses several advanced characteristics, e.g., high rupture strength, low weight, high corrosion resistance, and ease of usage. FRP bars have increasingly been considered an alternative to steel bars [2], especially in corrosive environments. Therefore, FRP has increasingly gained great attention from researchers and engineers. FRP has also been demonstrated as a successful material for retrofitting structures [3].

Although the design of FRP RC components has been adopted in standards such as CSA [4] and ACI 440.1R-15 [5], FRP RC is still reluctant to be used for structures in practice because 1) FRP rebars have a lower elastic modulus than steel, leading to larger cracks and deflections; 2) the failure mode of FRP bars is brittle failure, which is an unfavorable characteristic because less failure warning is provided before the failure. Hybrid FRP-steel RC structures appear to be a good solution because they take advantage of the high ductility of steel and the high tensile strength and non-corrosion of FRP.

Hybrid FRP-steel RC beams have been a research topic that attracted several researchers. Maria and Ombres [6] reported that the width and spacing of cracks of steel RC beams is less than those of Aramid FRP (AFRP) RC beams. In addition, the addition of steel to the AFRP reinforcement increased the ultimate strength by less than 15% the ultimate strength due to the compressive failure of concrete. Deflections of FRP-steel RC beams were predicted by Bischoff [7, 8] and Bischoff and Scanlon [9]. Glass FRP (GFRP) RC beams had high deflection capacity, although they failed in brittle compression [10]. Hybrid GFRP-steel RC beams had good ductility, durability, and serviceability [11]. Ductility of hybrid FRP-steel RC beams was higher than that of FRP RC beams [12]. The arrangement of GFRP and steel bars at the outer layer resulted in the highest ultimate load-carrying capacity for GFRP-steel RC beams [13]. Ductility and stiffness of FRP-steel RC beams improved because of the presence of steel in the reinforcement [14]. Hybrid GFRP-steel RC beams had higher strength and ductility than GFRP RC beams [15]. The decrease in BFRP-to-steel area ratio reduced the deflection and crack spacing when the hybrid BFRP-steel RC beams were subjected to a similar load [16]. GFRP resulted in better ductility for FRP-steel RC beams than any other FRP type [17]. Yoo et al. [18] found that stiffness and strength of hybrid GFRP-steel reinforced ultra-high-performance fiber-reinforced concrete beams increased as the GFRP ratio increased. In

addition, the preyield stiffness and postyield stiffness of hybrid beams were higher and lower than those of GFRP RC beams, respectively. Qin et al. [19] recommended GFRP-to-steel area ratios of 1.0–2.5 to achieve desirable strength and ductility for hybrid FRP-steel RC beams. The increase in GFRP ratio in the regions of positive and negative moments reduced the ductility but increased the strength of continuous GFRP-steel RC beams [20]. Low-BFRP-ratio RC beams had more cracks than steel RC beams, while the deformation of BFRP RC beams was acceptable [21]. Hybrid FRP-steel RC beams had satisfactory strength and high ductility when the FRP-to-steel ratio was low [22]. The ductility of hybrid GFRP-steel RC beams was larger than 6, classified to be highly ductile, despite the brittle failure of concrete compression [23]. Concrete beams reinforced with hybrid steel FRP composite bars had higher ductility than hybrid BFRP-steel RC beams [24]. Ruan et al. [25] indicated that the ultimate strength of hybrid GFRP-steel RC beams was about 3%–9% lower than that of steel RC beams, but the stiffness was significantly decreased although they had the same reinforcement ratio. The serviceability and ductility of hybrid beams increased with the increase in the steel area [26]. Recently, Liu et al. [27] found that the crack width of hybrid BFRP-steel RC beams was 40% less than that of a steel RC beam. Sun et al. [28] proposed a method to predict the deformation capacity of hybrid BFRP-steel RC beams. Cao et al. [29] predicted the flexural and serviceability behavior of GFRP-stainless steel RC beams using the finite element method.

Along with the requirement of high corrosion resistance, structures are also required to have high strength and ductility. To balance these requirements, hybrid FRP-steel RC structures seem reasonable and are thus targeted by this study. Although a number of studies have been performed on hybrid FRP-steel RC beams, they have focused on specific ratios of reinforcement because of the nature of experimental investigations. In the literature, finite element modelling or theoretical analysis seems to inadequately focus on a full range of FRP-steel combinations. Furthermore, it appears to hardly find publications on the assessment of key parameters on the behavior and moment capacity of hybrid GFRP-steel RC beam sections. In addition, the effect of the ratio $\rho_{f/fs}$ of FRP area to the total area of reinforcement (varying from 0 to 1) on the behavior and moment capacity seems to be missing in the literature. Therefore, a systematically parametric investigation rather than isolated ratios used in experiments should be encouraged. In the above context, this study assesses the effect of key parameters and $\rho_{f/fs}$ on the moment–curvature behavior and ultimate moment of hybrid GFRP-steel RC beam sections. The research results can additionally provide some technical information for designing hybrid GFRP-steel RC beams in practice.

2 Fiber-model analysis and verifications

2.1 Description of tested hybrid GFRP-steel RC beams

The hybrid GFRP-steel RC beams tested by Ruan et al. [25] are revisited. The cross sections of the beams were 180 mm in width and 300 mm in height. The length of these beams was 1800 mm. Three beam sections, namely 2G12-2S12, 2G12-1S16, and 2G16-1S16 were selected for the modelling in this study. GFRP bars ϕ12 and ϕ16 were used. The tensile strength and elastic modulus of GFRP 12 mm were 868.22 MPa and 40.06 GPa, respectively. The tensile strength and elastic modulus of GFRP 16 mm were 958.20 MPa and 45.69 GPa, respectively. The steel bar ϕ12 had a yield strength of 517 MPa and an ultimate strength of 631.00 MPa. The steel bar ϕ16 had a yield strength of 540 MPa and an ultimate strength of 643.00 MPa. The elastic modulus of these steel bars was 200 GPa. Concrete had a compressive strength of 30.32 MPa. The beams were tested using 4-point loading. The span length was 1600 mm, and the distance between the two loads $P/2$ was 600 mm. The concrete cover measured to the outer surface of the longitudinal bars was 30 mm. The stirrups were ϕ8 with a spacing of 100 mm. These stirrups were arranged at 600 mm from the beam ends, while no stirrup was designed at 600 mm at the mid-span.

2.2 Fiber-model analysis

The stress–strain model of concrete proposed by Hognestad [30] (Figure 1a) was used. Elastic perfectly-plastic stress–strain model of steel [31] (Figure 1b) was adopted. The ultimate strain ε_u = 0.05 was used for steel reinforcement. The elastic modulus of steel was $E_s = 2\times10^5 MPa$. The stress–strain relationship of GFRP bars is linear up to the ultimate point ($\varepsilon_{u,gfrp}$, $f_{u,gfrp}$), in which $f_{u,gfrp}$, $\varepsilon_{u,gfrp} = f_{u,gfrp}/E_{gfrp}$, and E_{gfrp} are the ultimate strength, the ultimate strain, and elastic modulus of GFRP bars. For simplification, bond-slip issue between the reinforcement and concrete was ignored [32].

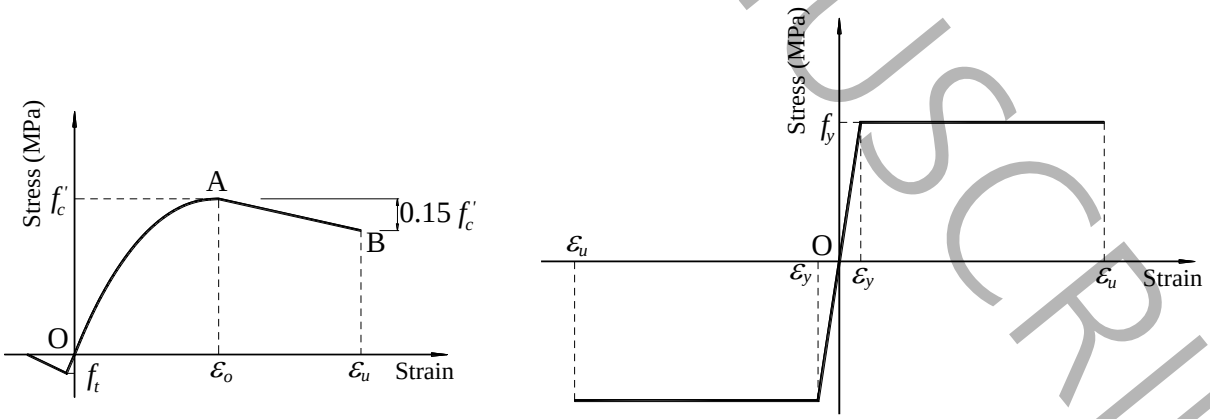

a) Model of concrete [30] b) Model of steel [31]

Figure 1. Stress–strain models of concrete and steel.

Sections of selected beams were modelled in SAP2000 [33] based on the fiber model (Figure 2).

The cross sections were divided into several small fibers, and these fibers are considered to be under axial loading. The plane strain assumption was adopted. The procedure of the analysis is briefly described here. At a particular curvature; the strains of all fibers were determined. These strains were used to determine the stress for those fibers. Consequently, the axial forces of those fibers were determined. The neutral axis was determined using the equilibrium of force. When the neutral axis was determined, the moment was computed. The procedure was repeated when the ultimate strains of the materials were reached.

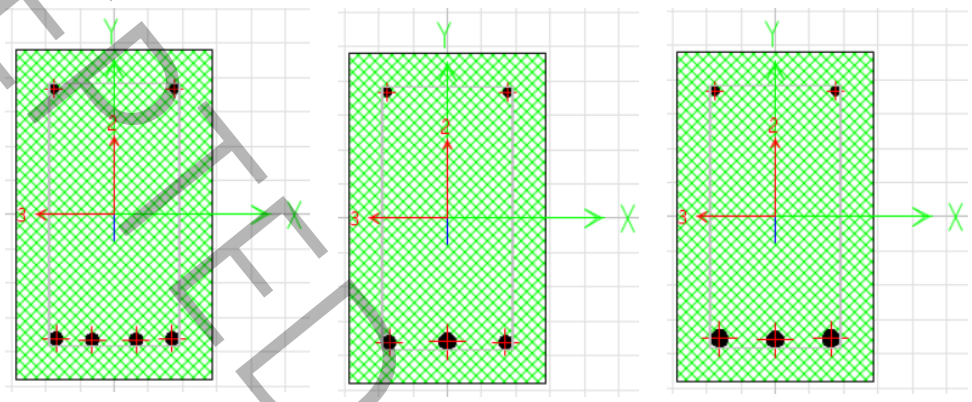

a) 2G12-2S12 b) 2G12-1S16 c) 2G16-1S16

Figure 2. Beam sections modelled in SAP2000 [33].

2.3 Results and verifications

Figure 3 shows moment–curvature curves of the analyzed sections in Section 4.1. It can be seen that the moment–curvature curves are affected by $\rho_{f/fs}$. When the section is dominated by steel bars ($\rho_{f/fs}$ is less than 0.5), the yield point is clearly exhibited. However, when the section is dominated by GFRP bars ($\rho_{f/fs}$ is less than 0.5), the yield point is not exhibited, and the moment-curvature curve is almost linear up to the ultimate point. This phenomenon is later clarified by consideration of different parameters in Section 5.

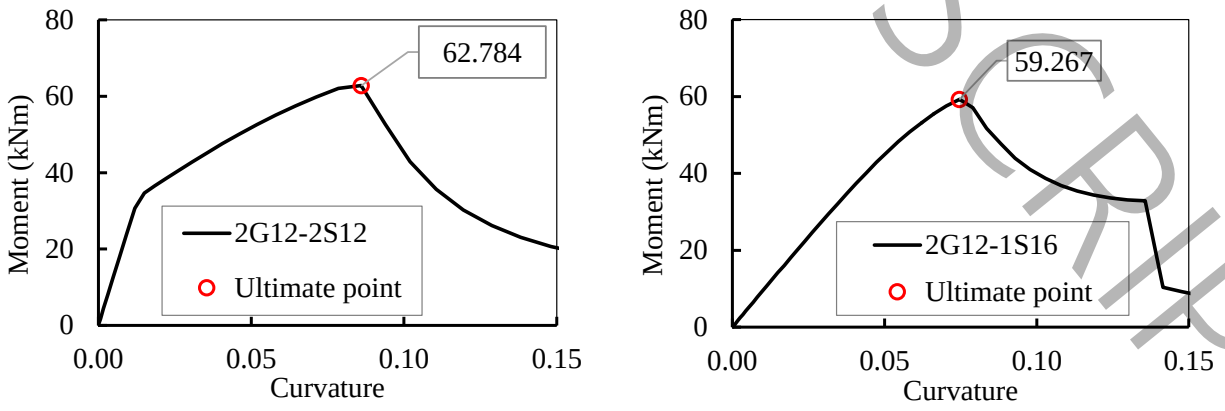

a) 2G12-2S12 b) 2G12-1S16

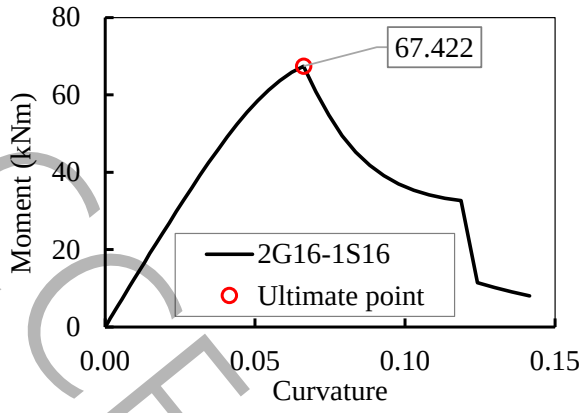

c) 2G16-1S16

Figure 3. Moment–curvature curves of sections

The ultimate moments obtained from SAP2000 models are presented in Table 1. The experimental results are also presented for comparisons. The analytical ultimate moments of sections 2G12-2S12, 2G12-1S16, and 2G16-1S16 were 62.8 kNm, 59.3 kNm, and 67.4 kNm, respectively. The experimental ultimate moments of these sections are 57.5 kNm, 56.4 kNm, and 66.7 kNm. Therefore, the differences between the analytical ultimate moment and the experimental ultimate moment are 9.2%, 5.1%, and 1.1%, respectively. The mean absolute percentage error (MAPE) is 5.13% and the root mean square error (RMSE) is 3.5 kNm, showing satisfactory approximations.

Table 1. SAP2000 vs experimental ultimate moments of the sections.

Beam section	Ultimate moment (kNm)		Difference (%)
	SAP2000	Experiment	
2G12-2S12	62.8	57.5	9.2
2G12-1S16	59.3	56.4	5.1
2G16-1S16	67.4	66.7	1.1

3 Effects of parameters on ultimate moment capacity

The section with the reinforcement of 2G12-2S12 was selected for parametric study. The total area of GFRP and steel reinforcement is 452.4 mm^2. To investigate the variations in the ultimate moment and the moment-curvature behavior of beam sections, the ratio $\rho_{f/fs}$ was selected to vary from 0 to 1 with the same interval of 0.05. The areas of GFRP and steel were calculated based on the ratio $\rho_{f/fs}$, then the diameter for two similar bars was calculated accordingly. For example, when $\rho_{f/fs}$ = 0.3, the areas of steel and GFRP are 316.7 mm^2 and 135.7 mm^2, respectively. Consequently, the diameters of two steel bars and two GFRP bars are 14.199 mm and 9.295 mm, respectively, for assigning in SAP2000. It is noted that these diameters do not conform with the real diameters of GFRP and steel

bars in practice; however, these diameters can be used to examine the variations in the moment–curvature and ultimate moment of hybrid GFRP-steel beam sections with respect to $\rho_{f/fs}$ when the compressive strength of concrete, yield strength of steel, and elastic modulus of GFRP are at constant values.

3.1 Effect of $\rho_{f/fs}$ on the behavior and ultimate moment

This section presents the results of section 2S12-2G12 when the material properties and the total area of reinforcement are kept constant. The considered variable is $\rho_{f/fs}$, which varies from 0 to 1. Figure 4 shows the moment–curvature curves of the section with twenty-one combinations of GFRP bars and steel bars. For the sake of vision, the curves of sections with $\rho_{f/fs}$ of 0.0, 0.25, 0.50, 0.75, and 1.00 are plotted in color, while the curves of other sections are plotted in black. When $\rho_{f/fs}$ is 0, the moment–curvature curve exhibits a yield point, clearly dividing the curve into two branches: elastic and plastic branches. Additionally, the curve has the highest elastic stiffness but the lowest plastic stiffness. When $\rho_{f/fs}$ increases, the yield moment and the elastic stiffness decrease while the plastic stiffness and ultimate moment increase. When $\rho_{f/fs}$ approaches 1.0, the elastic branch and the plastic branch merge into a straight line, and the yield point diminishes. The ultimate moment of section reinforced with only GFRP bars is highest. These observations can be helpful in selecting appropriate values of $\rho_{f/fs}$ depending on the design objective, which should take into account the elastic stiffness, plastic stiffness, and the ultimate moment. The curves intersect at a point, which can be named as a pivot point. This pivot point on the moment–curvature curves can be explained by the intersection point of the stress-strain curves of steel and GFRP. When $\rho_{f/fs}$ increases, the moment–curvature curves before and after the pivot point become lower and higher, respectively.

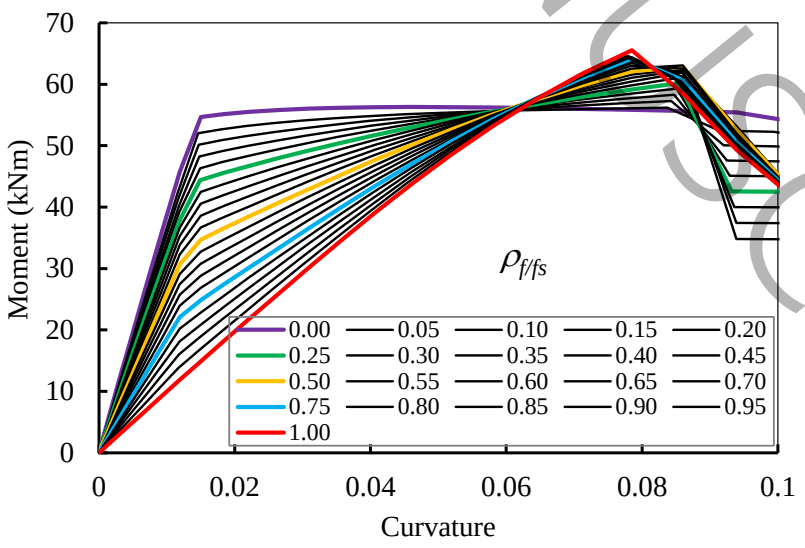

Figure 4. Effect of $\rho_{f/fs}$ on moment–curvature behavior

Figure 5 shows the variation in the ultimate moment with respect to $\rho_{f/fs}$. The ultimate moment increases with the increase in $\rho_{f/fs}$. When $\rho_{f/fs}$ is 0, the ultimate moment is the lowest at 56.3 kNm. When $\rho_{f/fs}$ = 1.0, the ultimate moment is the highest at 65.5 kNm, which is 16.3% higher than the ultimate moment of the section with $\rho_{f/fs}$ of 0. The increasing trend is approximated by the equation y = 8.8409x + 57.448. The increase in the ultimate moment is 0.884 kNm per 0.1 value of $\rho_{f/fs}$ for the considered section. This result indicates the positive effect of GFRP bars on the ultimate moment capacity of the beams.

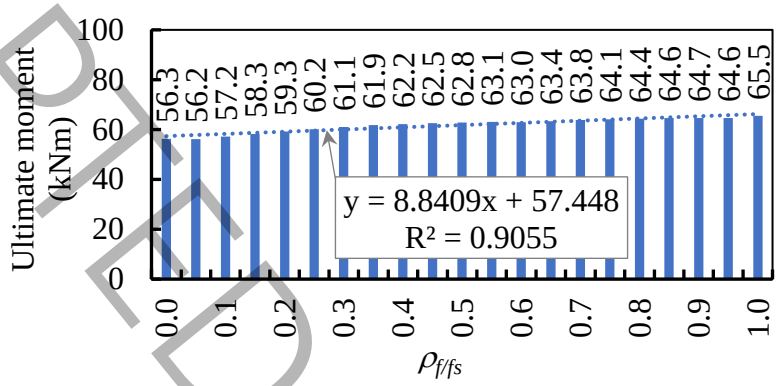

Figure 5. Effect of $\rho_{f/fs}$ on ultimate moment

3.2 Effect of yield strength of steel

Figures 6a–d show the moment–curvature curves of the sections with the steel strengths of 300 MPa, 400 MPa, 500 MPa, and 600 MPa, respectively. The axis limits of these figures are similar for visual comparison. The total area of reinforcement and other material properties were kept unchanged, while $\rho_{f/fs}$ varies from 0 to 1. The phenomenon of moment-curvature behavior mentioned in the previous section is clearly observed in this figure. The bilinear behavior of the section with $\rho_{f/fs}$ of 0 changes to the linear behavior of the section with $\rho_{f/fs}$ of 1. In addition, the steel strength plays an important role in the effectiveness of GFRP bars. When the steel strength is low, e.g., f_y = 300 MPa, the increase in $\rho_{f/fs}$ effectively improves the ultimate moment (Figure 6a). However, when the steel strength is high, e.g., f_y = 600 MPa, the ultimate moments of sections are almost similar regardless of the ratio $\rho_{f/fs}$ (Figure 6d). In addition, the ultimate points of these curves are around at the intersection point. This is simply due to the fact that f_y = 600 MPa is nearly close to the ultimate tensile strength of GFRP.

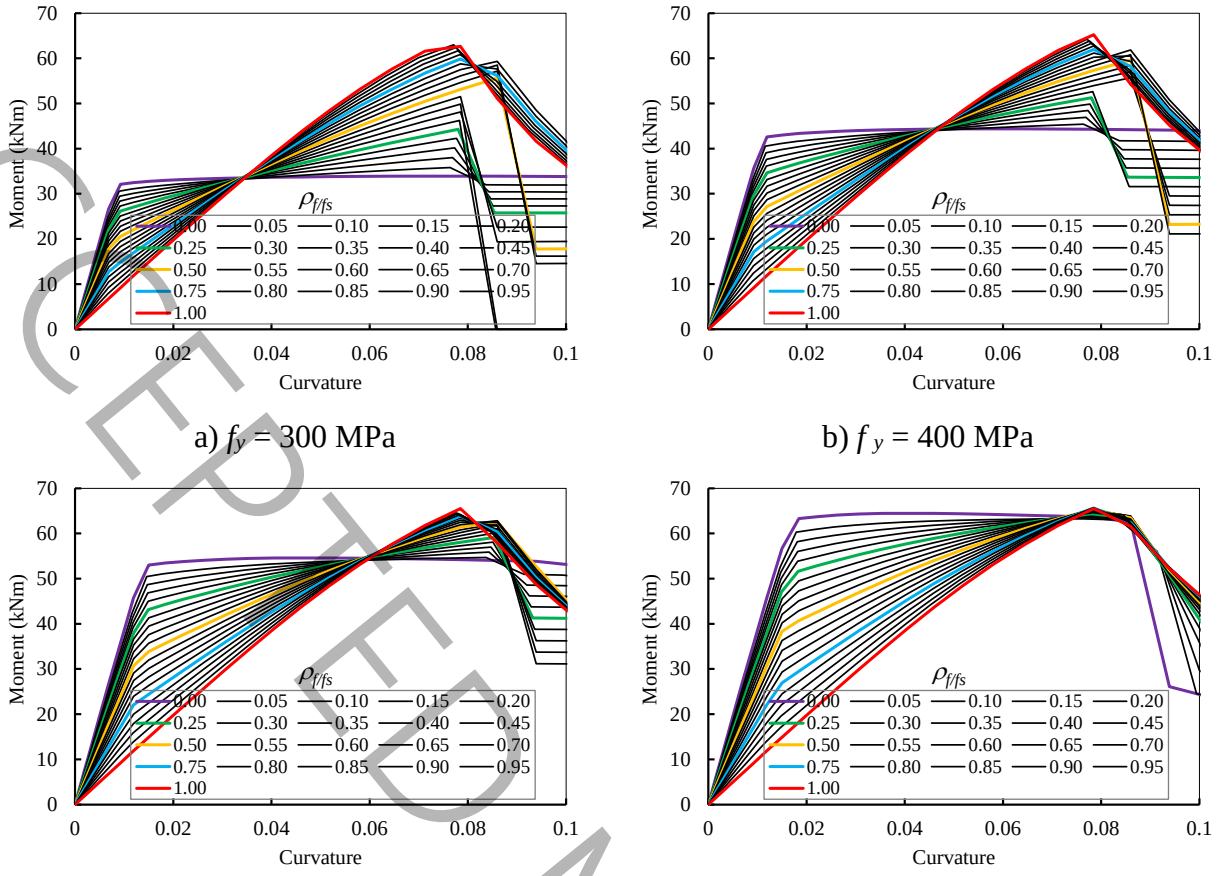

a) f_y = 300 MPa b) f_y = 400 MPa

c) f_y = 500 MPa d) f_y = 600 MPa

Figure 6. Effect of yield strength of steel on moment–curvature behavior

Figure 7 shows the variation in the ultimate moment versus $\rho_{f/fs}$ when the steel yield strengths were 300, 400, 500, and 600 MPa. The trend lines of these ultimate moments are also plotted. Although these trend lines are different, they intersect at the point when $\rho_{f/fs}$ = 1. This is because, when $\rho_{f/fs}$ = 1, the sections become one section, which is reinforced with only GFRP bars. In other words, steel bars do not exist in the section when $\rho_{f/fs}$ = 1. Overall, the ultimate moment increases as $\rho_{f/fs}$ increases. The trend line of the section with a yield strength of steel of 300 MPa is the lowest but with the highest slope coefficient of 30.481 kNm per unit of $\rho_{f/fs}$. The slope coefficient reduces as the steel yield strength increases. When the yield strengths of steel are 400 MPa and 500 MPa, the slope coefficients are 20.997 and 10.4 kNm per unit of $\rho_{f/fs}$, respectively. The slope coefficient is lowest at 1.9282 kNm per unit of $\rho_{f/fs}$ when the yield strength of steel is 600 MPa. The slope coefficient of a section with steel with a yield strength of 300 MPa is approximately 15 times greater than that of a section reinforced with steel with a yield strength of 300 MPa. These findings indicate the important role of GFRP bars in effectively replacing the steel reinforcement when the yield strength of steel is low. However, when the yield strength of steel is relatively high, GFRP bars seem to be less effective in replacement of steel bars. It is noted that this replacement is based on the

criterion of the same cross-sectional area. The above-mentioned phenomenon can be explained by the fact that the increase in the yield strength of steel make it approach the tensile strength of GFRP. Consequently, the pivot point of the moment–curvature curves also is shifted toward the ultimate point, reducing the effectiveness on increasing the moment capacity when $\rho_{f/fs}$ increases.

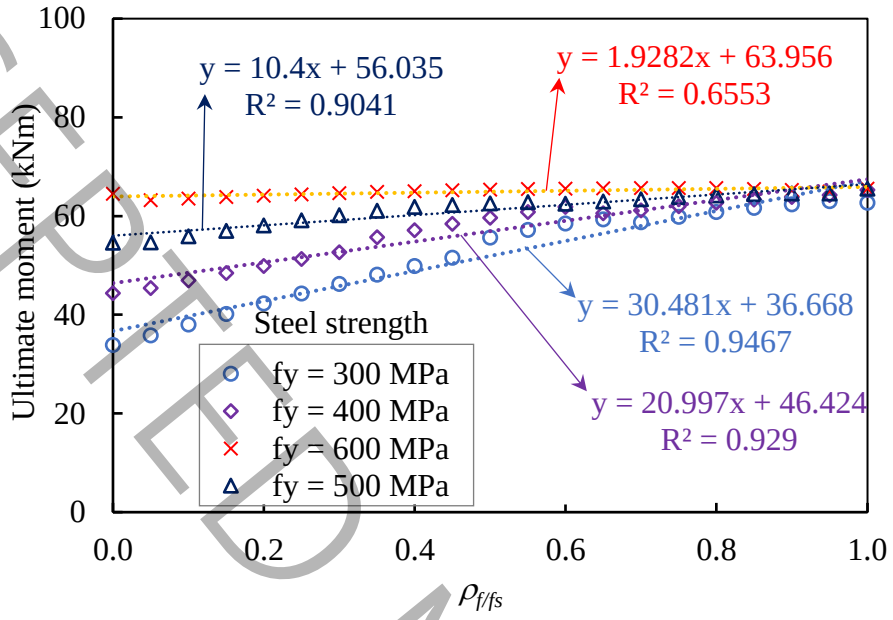

Figure 7. Effect of yield strength of steel on ultimate moment

3.3 Effects of elastic modulus of FRP

Figure 8 shows the moment–curvature curves of the section with different $\rho_{f/fs}$. It is noted that the material properties were kept unchanged while the elastic modulus of GFRP bars was 40, 45, 50, and 55 MPa. These elastic moduli were selected around the common value of 45–50 MPa of GFRP bars. Figure 8 indicates that the elastic modulus of GFRP marginally affects the moment–curvature behavior of the section. The phenomenon of pivot point also exhibits.

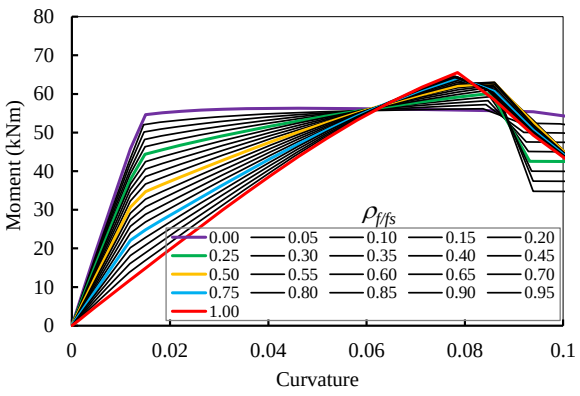

a) E_f = 40 MPa

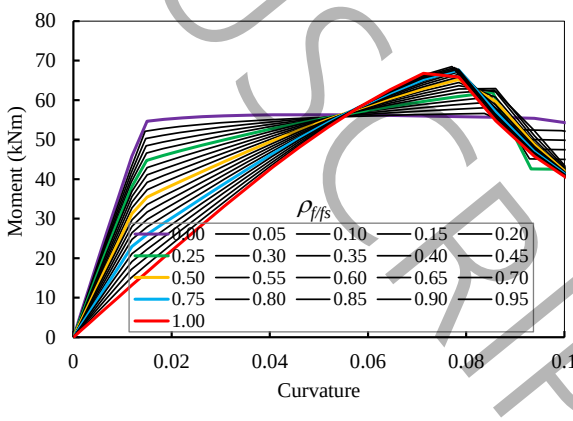

b) E_f = 45 MPa

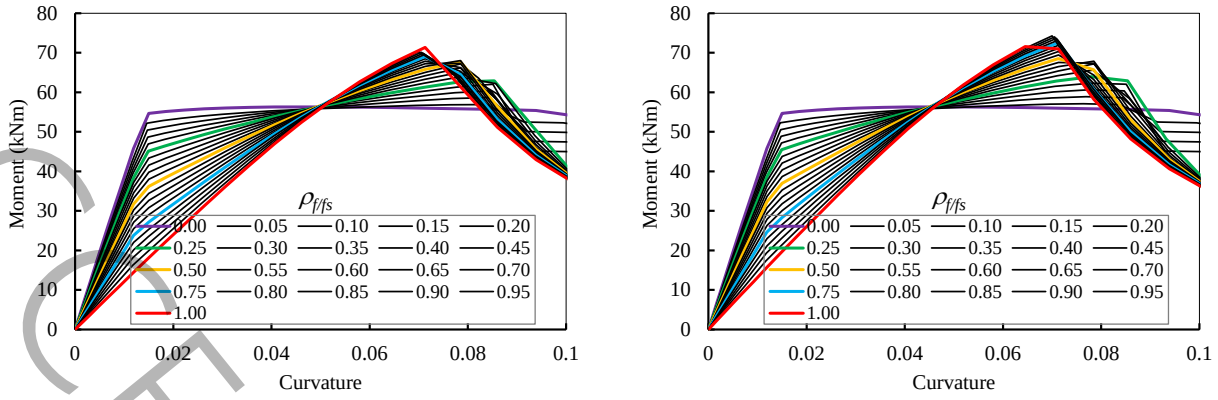

c) E_f = 50 MPa d) E_f = 55 MPa

Figure 8. Effect of elastic modulus of FRP on moment–curvature behavior

Figure 7 shows the variation in the ultimate moment of the section with a specific value of the elastic modulus of GFRP when $\rho_{f/fs}$ varies from 0 to 1. The trend lines with equations are also plotted. Generally, the increase in the elastic modulus of GFRP slightly increases the ultimate moment. In addition, with a specific elastic modulus, increasing $\rho_{f/fs}$ increases the ultimate moment. The slope coefficients are 8.84, 12.03, 13.90, and 17.43 kNm per unit of $\rho_{f/fs}$. The slope coefficient for the section with an elastic modulus of GFRP of 55 MPa is almost twice that of 40 MPa. This finding is for reference in the effect of elastic modulus of GFRP on the ultimate moment of the hybrid GFRP-steel RC section. In practice, it may be difficult to select the elastic modulus of GFRP as it is manufactured in a factory; however, this result may be a recommendation for selecting the FRP type with a higher elastic modulus to improve the ultimate moment capacity of beam sections.

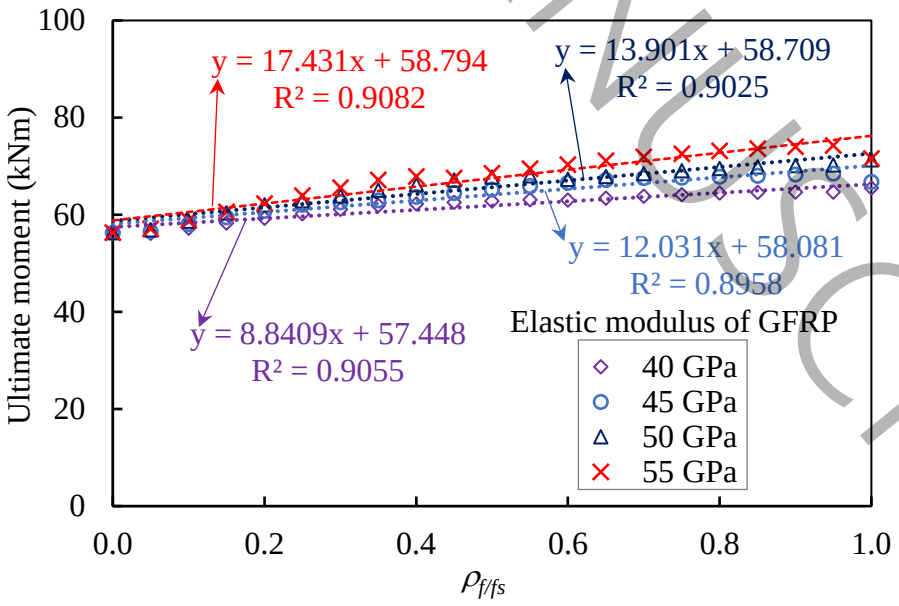

Figure 9. Effect of elastic modulus of GFRP on ultimate moment

3.4 Effect of compressive concrete strength

Figures 10a–d show the moment–curvature curves of sections with different compressive concrete strengths of 30 MPa, 40 MPa, 50 MPa, and 60 MPa, respectively. The phenomenon of pivot point is also observed. When the compressive strength of concrete is 30 MPa, the compression failure of concrete occurs at the ultimate point, resulting in a decrease in the moment. When the compressive concrete strength increases to 40 MPa, 50 MPa, and 60 MPa, the ultimate point of the sections is governed by the rupture of GFRP bars, resulting in a sharp drop of the moment. When $\rho_{f/fs}$ increases from 0 to 1, the bilinear behavior changes to linear behavior, and the ultimate load increases.

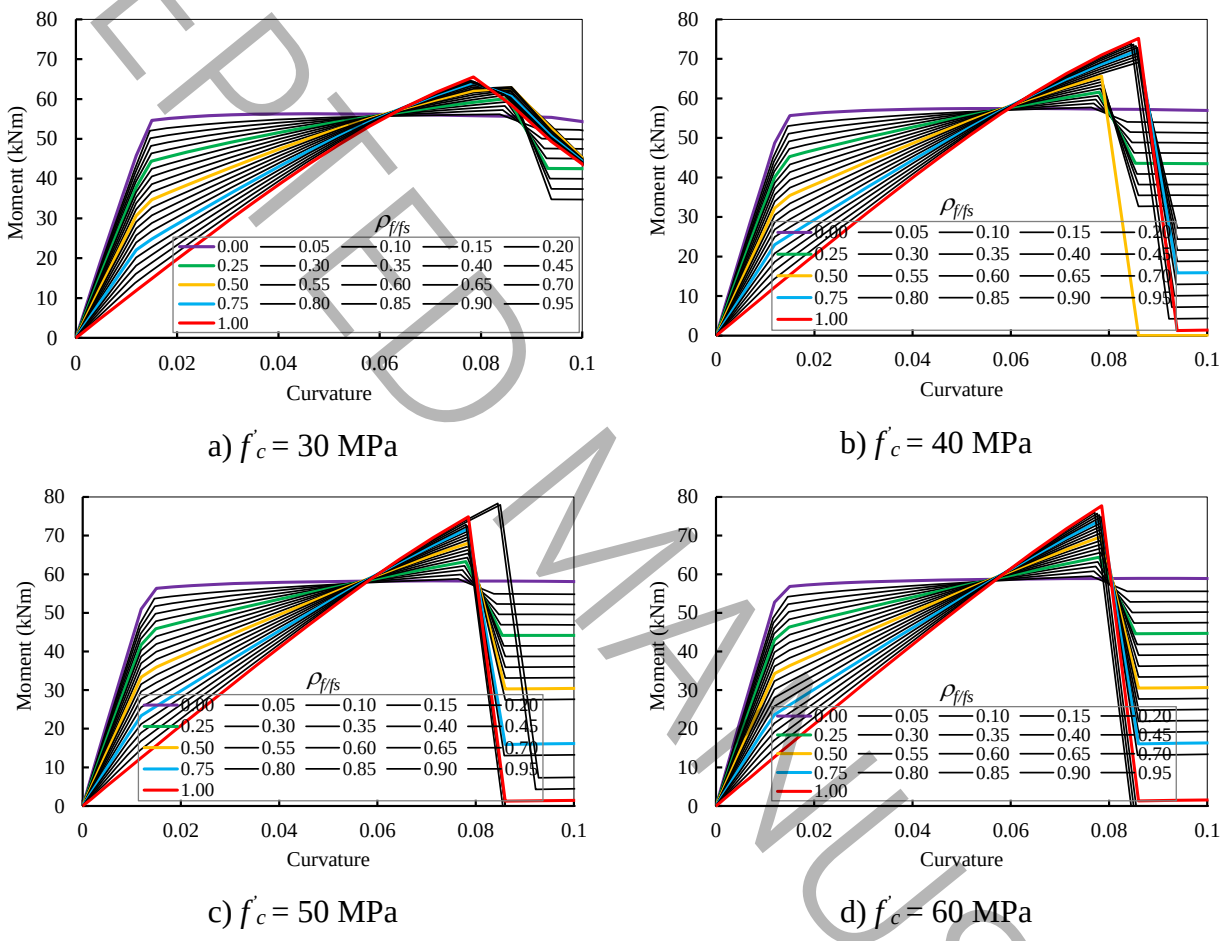

a) f'_c = 30 MPa

b) f'_c = 40 MPa

c) f'_c = 50 MPa

d) f'_c = 60 MPa

Figure 10. Effect of compressive concrete strength on moment–curvature behavior

Figure 11 presents variations in the ultimate moment of concrete sections reinforced with different GFRP-steel combinations when the compressive strengths of concrete were 30 MPa, 40 MPa, 50 MPa, and 60 MPa. When $\rho_{f/fs}$ is 0, the ultimate moments are close to one another. When $\rho_{f/fs}$ is 1, the ultimate moments exhibit a larger difference. Particularly, the ultimate moment of the section with concrete strength of 30 MPa is lower than those of sections with concrete strength of 40 MPa, 50 MPa, and 60 MPa. This is attributed to the fact that sections with high strength of concrete fail by rupture of the tension reinforcement. This tension failure can be evidenced in Figures 10b–d: the curves drop sharply after the ultimate point. In contrast, the failure of sections with concrete strength

of 30 MPa (Figure 10a) is the compression failure, in which the ultimate moment slowly decreases after the ultimate point. Therefore, concrete with higher compressive strength can better exploit the strength of tensile reinforcement. In the context of increasing the compressive concrete strength while keeping other parameters as constant, the compression resistance increases while the tension resistance remains unchanged. With low compressive concrete strength, the demand compression force reaches the compression resistance of concrete before the demand tension force reaches the tension resistance of the reinforcement (leading to compressive failure). When the compressive concrete strength increases and other parameters are kept constant, the compression resistance of concrete increases. Consequently, the demand compression force reaches the compression resistance of concrete after the demand tension force reaches the tension resistance of the reinforcement (leading to compressive failure). The failure mode shifted from compression failure to tensile rupture as evidenced by the curve portion after the ultimate point. As the compressive strength increases (going from Figure 10a to Figure 10d), the drop of the curve becomes stronger.

Despite the above difference in the ultimate moments and the failure modes due to the compressive strength of concrete, the ultimate moment increases with the increase in $\rho_{f/fs}$. This finding indicates the greater effectiveness of GFRP than steel in reinforcing the concrete beams in terms of ultimate moment. When the compressive strength of concrete is 30 MPa, the increasing rate is lowest at 8.84 kNm per unit of $\rho_{f/fs}$. The increasing rates are 19.13, 18.82, and 18.85 kNm per unit of $\rho_{f/fs}$ when the compressive strengths of concrete are 40, 50, and 60 MPa, respectively. These increasing rates are close to one another. Their average is 18.93 kNm per unit of $\rho_{f/fs}$, which is 2.14 times that of the case of compressive strength of 30 MPa. This result also indicates the greater effectiveness of GFRP when it works with high-strength concrete. This is explained by the fact that high-strength concrete reduces compressive strain, which in turn increases the tensile strain of GFRP; consequently, the tensile strength of GFRP is better exploited. Therefore, high-strength concrete should be used to make hybrid GFRP-steel or GFRP RC beams.

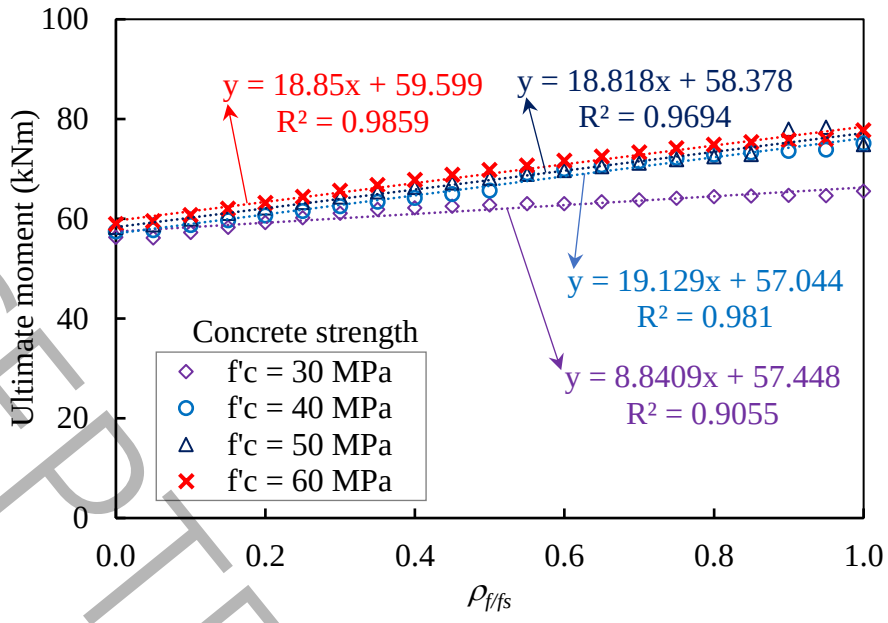

Figure 11. Effect of compressive concrete strength on the ultimate moment

3.5 Comparing the effects of the considered parameters

The effects of the considered parameters are compared in this subsection. To achieve this aim, the average trend lines are computed and plotted in the coordinate system, in which the horizontal axis is $\rho_{f/fs}$ and the vertical axis is the ultimate moment. The average trend line is expressed by $y = a_e x + b_e$, in which a_e is the average coefficient of the four coefficients and b_e is the average intercept of the four intercepts. The obtained average trend lines are plotted in Figure 12 for comparison. It can be seen that the compressive strength exhibits an important parameter, resulting in the highest ultimate moment. In contrast, the yield strength of steel seems to be the least important parameter in the ultimate moment. However, low $\rho_{f/fs}$ results in higher ductility for the hybrid GFRP-steel RC sections.

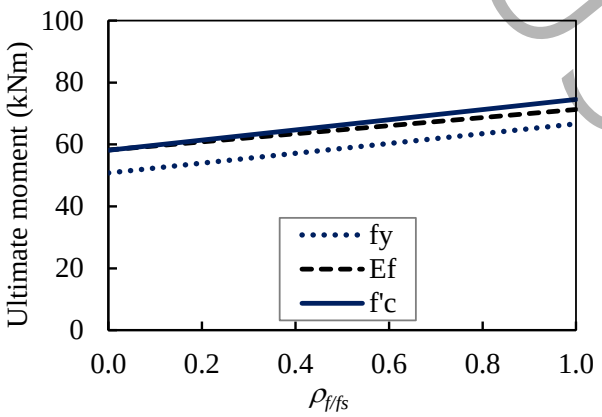

Figure 12. Comparison of the average trend lines

4 Multivariate linear regression

The data of section 3 were used for multilinear regression analyses. The data include the ultimate moment (M_u) and four variables. These four variables are the yield strength of steel (f_y), compressive strength of concrete (f'_c), and the elastic modulus of GFRP (E_f), while $\rho_{f/fs}$ varies from 0 to 1. Open-source software R was used to process and analyze the data. This software conducts multivariate regression based on the Bayesian model average (BMA) method. The dependent variable is the ultimate moment (M_u). Other variables are $x_1 = f_y$, $x_2 = \rho_{f/fs}$, $x_3 = f'_c$, and $x_4 = E_f$. Table 2 shows the best model obtained from the multivariate linear regression. Column 1 of this table presents the independent variables. The probability of the regression coefficients and the expected values of variables are presented in columns 2 and 3, respectively. Column 4 presents the standard deviations of variables. The last column presents parameters for the model of ultimate moment. This model is expressed by Equation 1. Table 2 shows that the model has R^2 value of 0.865, showing a good correlation. The model expressed by Equation 1 indicates that the considered parameters have positive effects on the ultimate moment.

Table 2. Model of ultimate moment with respect to $x_1 - x_4$

	p!=0	Estimated Value	Standard deviation	model 1
Intercept	100	8.522	1.96345	8.522
x_1	100	0.0451	0.00238	0.0451
x_2	100	15.137	0.54455	15.137
x_3	100	0.266	0.01852	0.266
x_4	100	0.365	0.03678	0.365
Number of variables				4
R^2				0.865
Bayesian Information Criteria (BIC)				-482.07
Posterior probability				1

$$M_u = 0.0451x_1 + 15.137x_2 + 0.266x_3 + 0.365x_4 + 8.522 \quad (1)$$

5 Conclusions

In this study, hybrid GFRP-steel beam sections were selected, and fiber models were developed. These models were verified by comparing their results with the experimental results with satisfactory approximations. The fiber models were used for investigations of the moment–curvature behavior and ultimate moment in relation with four considered variables. These considered parameters were the yield strength of steel (f_y), compressive strength of concrete (f'_c),

the elastic modulus of GFRP (E_f), and $\rho_{f/fs}$ (varying from 0 to 1). Conclusions are made as follows.

- $\rho_{f/fs}$ significantly affects the moment–curvature behavior. The yield point is distinct when $\rho_{f/fs}$ = 0, and it diminishes when $\rho_{f/fs}$ = 1. When $\rho_{f/fs}$ increases from 0 to 1, the bilinear response transitions to a linear response, and the ultimate moment increases
- A pivot point phenomenon was observed in the moment–curvature curves when $\rho_{f/fs}$ varied from 0 to 1. When the demand curvature is less than the curvature of the pivot point, the moment of section with low $\rho_{f/fs}$ is higher than that of section with high $\rho_{f/fs}$. These become inverted when the demand curvature is larger than the pivot curvature.
- Concrete strength exhibited a significant role in the ultimate moment of hybrid GFRP-steel RC beams. Concrete with higher compressive strength more effectively exploits the tensile strength of GFRP bars due to the compression failure of concrete.
- GFRP bars can effectively replace low-strength steel bars, resulting in higher ultimate moment. For high-strength steel bars, GFRP replacement results in a comparable ultimate moment. The effectiveness of the replacement improves when GFRP bars with a higher elastic modulus are used.
- A multivariate regression analysis was conducted, yielding a predictive model of ultimate moment with good correlations (R^2 = 0.865). The model indicates that the yield strength of steel, compressive strength of concrete, elastic modulus of GFRP, and $\rho_{f/fs}$ exhibit positive effects on the ultimate moment.

Acknowledgements

This research is funded by Vietnam National University HoChiMinh City (VNU-HCM) under grant number: **B2024-20-08**.

References

[1] H. Zhou, S. Chen, Y. Du, Z. Lin, X. Liang, J. Liu, F. Xing, Field test of a reinforced concrete bridge under marine environmental corrosion, Engineering Failure Analysis, 115 (2020) 104669.

[2] s. vakili, p. homami, M.R. esfahani, Experimental Investigation of the Effect of Hybrid fibers on Lightweight Concrete Beams Reinforced with GFRP Bars, AUT Journal of Civil Engineering, 3(2) (2019) 233-242.

[3] O. Yousefi, Numerical Investigation on Structural Behaviors of Deficient Steel CHS Long Columns Strengthened Using CFRP %J AUT Journal of Civil Engineering, 6(4) (2022) 509-520.

[4] CanadianStandardsAssociation, Design and construction of building structures with fibre-

reinforced polymers (CSA S806), in, Rexdale 2012.

[5] ACI, ACI 440.1R-15. Guide for the design and construction of structural concrete reinforced with Fiber-Reinforced Polymer (FRP) bars, in, Farmington Hills, MI 48331, 2015.

[6] M.A. Aiello, L. Ombres, Structural Performances of Concrete Beams with Hybrid (Fiber-Reinforced Polymer-Steel) Reinforcements, Journal of Composites for Construction, 6(2) (2002) 133-140.

[7] P.H. Bischoff, Reevaluation of Deflection Prediction for Concrete Beams Reinforced with Steel and Fiber Reinforced Polymer Bars, Journal of Structural Engineering, 131(5) (2005) 752-767.

[8] P.H. Bischoff, Deflection Calculation of FRP Reinforced Concrete Beams Based on Modifications to the Existing Branson Equation, Journal of Composites for Construction, 11(1) (2007) 4-14.

[9] P.H. Bischoff, A. Scanlon, Effective Moment of Inertia for Calculating Deflections of Concrete Members Containing Steel Reinforcement and Fiber-Reinforced Polymer Reinforcement, ACI Structural Journal, 104(1) (2007) 68-75.

[10] C. Barris, L. Torres, A. Turon, M. Baena, A. Catalan, An experimental study of the flexural behaviour of GFRP RC beams and comparison with prediction models, Composite Structures, 91(3) (2009) 286-295.

[11] W. Qu, X. Zhang, H. Huang, Flexural Behavior of Concrete Beams Reinforced with Hybrid (GFRP and Steel) Bars, Journal of Composites for Construction, 13(5) (2009) 350-359.

[12] D. Lau, H.J. Pam, Experimental study of hybrid FRP reinforced concrete beams, Engineering Structures, 32(12) (2010) 3857-3865.

[13] L. Yinghao, Y. Yong, Arrangement of hybrid rebars on flexural behavior of HSC beams, Composites Part B: Engineering, 45(1) (2013) 22-31.

[14] I.F. Kara, A.F. Ashour, M.A. Köroğlu, Flexural behavior of hybrid FRP/steel reinforced concrete beams, Composite Structures, 129 (2015) 111-121.

[15] A. El Refai, F. Abed, A. Al-Rahmani, Structural performance and serviceability of concrete beams reinforced with hybrid (GFRP and steel) bars, Construction and Building Materials, 96 (2015) 518-529.

[16] W. Ge, J. Zhang, D. Cao, Y. Tu, Flexural behaviors of hybrid concrete beams reinforced with BFRP bars and steel bars, Construction and Building Materials, 87 (2015) 28-37.

[17] L. Pang, W. Qu, P. Zhu, J. Xu, Design Propositions for Hybrid FRP-Steel Reinforced Concrete Beams, Journal of Composites for Construction, 20(4) (2016) 04015086.

[18] D.-Y. Yoo, N. Banthia, Y.-S. Yoon, Flexural behavior of ultra-high-performance fiber-reinforced concrete beams reinforced with GFRP and steel rebars, Engineering Structures, 111 (2016) 246-262.

[19] R. Qin, A. Zhou, D. Lau, Effect of reinforcement ratio on the flexural performance of hybrid FRP reinforced concrete beams, Composites Part B: Engineering, 108 (2017) 200-209.

[20] A.M. Araba, A.F. Ashour, Flexural performance of hybrid GFRP-Steel reinforced concrete continuous beams, Composites Part B: Engineering, 154 (2018) 321-336.

[21] J. Duic, S. Kenno, S. Das, Performance of concrete beams reinforced with basalt fibre composite rebar, Construction and Building Materials, 176 (2018) 470-481.

[22] Y. Yang, Z.-Y. Sun, G. Wu, D.-F. Cao, Z.-Q. Zhang, Flexural capacity and design of hybrid FRP-steel-reinforced concrete beams, Advances in Structural Engineering, 23(7) (2019) 1290-1304.

[23] Z. Sun, L. Fu, D.-C. Feng, A.R. Vatuloka, Y. Wei, G. Wu, Experimental study on the flexural behavior of concrete beams reinforced with bundled hybrid steel/FRP bars, Engineering Structures, 197 (2019) 109443.

[24] Y. Yang, Z.-y. Sun, G. Wu, D.-f. Cao, D. Pan, Experimental study of concrete beams reinforced with hybrid bars (SFCBs and BFRP bars), Materials and Structures, 53(4) (2020) 77.

[25] X. Ruan, C. Lu, K. Xu, G. Xuan, M. Ni, Flexural behavior and serviceability of concrete beams hybrid-reinforced with GFRP bars and steel bars, Composite Structures, 235 (2020) 111772.

[26] H. Abbas, A. Abadel, T. Almusallam, Y. Al-Salloum, Experimental and analytical study of flexural performance of concrete beams reinforced with hybrid of GFRP and steel rebars, Engineering Failure Analysis, 138 (2022) 106397.

[27] S. Liu, X. Wang, M.S. Ali Yahia, C. Su, Z. Wu, Flexural Performance and Design of Concrete Beams Reinforced with BFRP and Steel Bars, Journal of Composites for Construction, 27(6) (2023) 04023062.

[28] Y. Sun, Z. Sun, J. Fu, X. Cai, G. Wu, Study on the deformation of hybrid BFRP-steel reinforced concrete beams considering crack development, Advances in Structural Engineering, 28(5) (2024) 919-938.

[29] Q. Cao, Z. Jia, C. Zhou, Flexural and serviceability behavior predictions of concrete beams

reinforced with hybrid reinforcement of GFRP bars and highly ductile stainless steel bars, Structures, 77 (2025) 109102.

[30] E. Hognestad, A study of combined bending axial load in reinforced concrete members, Engineering Experimental Station, The University of Illinois, Urbana, 1951.

[31] ACI, Building code requirements for structural concrete (ACI 318-19), in, American Concrete Institute, 38800 Country Club Drive, Farmington Hills, MI 48331, U.S.A., 2019.

[32] M. Tavakol, H. Haji Kazemi, Comparative assessment of concrete columns reinforced with hybrid steel-GFRP, GFRP, and steel bars under cyclic lateral loading, Structures, 71 (2025) 108034.

[33] Computers and Structures Inc, SAP2000 Version 19.2.0, (2017).